





Cite this: DOI: 10.1039/c7nr09645c

Packing of metalized polymer nanofibers for aneurysm embolization

 Min-Woo Kim,^{†a} Seongpil An,^{†a} Karam Kim,^a Tae-Gun Kim,^a Hong Seok Jo,^a
 Dong-Hyuk Park,^{*b} Sam S. Yoon ^{*a} and Alexander L. Yarin ^{*c}

Aneurysmal subarachnoid hemorrhage (SAH) is the extravasation of blood into the subarachnoid space and is fatal in most cases. Platinum coils have been used to fill the hemorrhage site and prevent the extravasation of blood. Here we explored the use of Pt-coated polymer nanofibers (NF) to prevent blood extravasation and were able to achieve improved results *in vitro*. The polymer nanofibers were produced via electrospinning and were subsequently electroplated with Pt, resulting in metalized nanofibers. These nanofibers were installed within a microfluidic channel, and the resulting reduction in the permeability was evaluated using a fluid similar to blood. Based on the obtained results, these newly developed nanofibers are expected to decrease the operation cost for SAH, owing to their reduced size and low material cost. Furthermore, it is expected that these nanofibers will be used in a smaller amount during SAH operation while having the same preventive effect. This should reduce the operational risk associated with the multiple steps required to place the Pt coils at the SAH site. Finally, the underlying hydrodynamic mechanism responsible for the reduced permeability of the synthesized nanofibers is described.

Received 27th December 2017,

Accepted 14th March 2018

DOI: 10.1039/c7nr09645c

rsc.li/nanoscale

1. Introduction

Aneurysmal subarachnoid hemorrhage (SAH), which is the extravasation of blood into the subarachnoid space,¹ has a high incidence rate, with tens of thousands of people in the United States alone being affected by it annually.^{2–6} Approximately, 5% of all the strokes are related to aneurysmal SAH. Furthermore, once it occurs, 40–44% of the patients are dead within 30 days and, of those who survive, 10–20% become disabled.^{2,3,7,8} In recent years, research interest in aneurysmal SAH has increased significantly because it is now known that aneurysmal SAH is more fatal to younger patients than to older ones.⁹ The expected first-year medical expense per patient for the treatment of SAH is 40 000–50 000 USD,^{10–12} while the corresponding total expense per patient is estimated to be greater than 200 000 USD.¹⁰

While both neurosurgical clipping and endovascular coiling have been used to treat cerebral aneurysms, endovascular coiling has become the more popular treatment after the development of Guglielmi detachable coils (GDCs) and the

corresponding derivative devices (*i.e.*, the guiding catheter).¹³ Furthermore, based on several reports,¹⁴ the American Society of Interventional and Therapeutic Neuroradiology, the American Society of Neuroradiology,¹⁵ and the German Society of Neurosurgery¹⁶ have also endorsed the use of the endovascular coiling treatment for patients with a ruptured cerebral aneurysm. More recently, the US Food and Drug Administration also approved the GDC treatment for all brain-related aneurysms.¹⁷

Endovascular coiling can be accomplished by inserting platinum (Pt) coils into the cerebral aneurysms, thus filling the aneurysmal cavity to prevent blood from flowing into the aneurysmal sac, as described in Fig. 1. However, even though endovascular coil embolization is preferred occasionally in the management of intracranial aneurysms,¹⁸ several factors need to be improved for endovascular coiling to find wider use. Depending on the size of the aneurysm, a number of coils may be required for the aneurysm coiling procedure.¹⁹ Another issue that needs to be overcome is incomplete embolization or recanalization. The recanalization rate for the treatment of aneurysms with bare Pt coils has been reported to be 4.7–28%.²⁰ During follow-ups, the coil packing density was found to be an important predictor of complete occlusion and is now used as an index to estimate the success of the initial procedure.

With the recent advancements in fabrication technologies, several types of endovascular coils have been developed beyond the classical bare Pt coils, including biopolymer-coated

^aSchool of Mechanical Engineering, Korea University, Seoul 02841, Republic of Korea. E-mail: skyoon@korea.ac.kr

^bDepartment of Neurosurgery, Korea University Anam Hospital, Korea University College of Medicine, Seoul, Republic of Korea. E-mail: doctorns@korea.ac.kr

^cDepartment of Mechanical and Industrial Engineering, University of Illinois at Chicago, Chicago, IL, USA. E-mail: ayarin@uic.edu

[†]These authors have equally contributed.

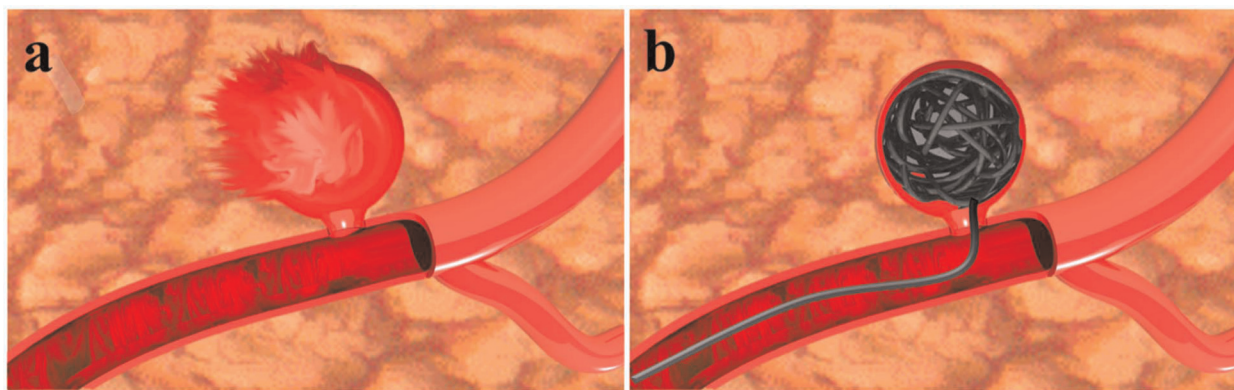


Fig. 1 Schematic of (a) aneurysm (after swelling of artery) and (b) embolization using Pt-coated nanofiber yarn.

coils and hydrogel-coated coils, among others. However, polymer-coated coils do not show any significant improvements over the bare Pt ones.^{21,22} Furthermore, hydrogel coils have several limitations such as a relatively high stiffness (Young's modulus of the 2% (w/v) alginate and 1% (w/v) agarose hydrogels is of the order of 10 kPa) as well as the time restrictions related to their placement.^{23,24} Thus, before assisting materials can be incorporated, specific materials and processes need to be developed for enhancing the coil packing density, which is defined as the ratio of the inserted coils to the volume of the formed aneurysm.¹⁹ This can be achieved by reducing the coil diameter, which, in turn, would increase the pressure drop across the coil-inserted aneurysm.²⁵

Recently, An *et al.* fabricated Pt-coated nanofibers by a simple and low-cost approach that combined electrospinning and electroplating; the diameter of the fabricated nanofibers was of the order of hundreds of nanometers.²⁶ The purity of the Pt-coated nanofibers was confirmed through various characterization techniques, and it was shown that the fibers have significant potential for use as an endovascular coil material. In the present study, Pt-coated polymer nanofibers were formed, and their packing performance was evaluated through microfluidic experiments. In addition, an analytical model of a coil-treated cerebral aneurysm was developed to quantitatively and qualitatively elucidate the effect of permeability as well as geometry changes on flow of the filtrating blood through a cerebral aneurysm. It was found that the fibers exhibited a higher packing density, owing to their small diameter, as compared to that of existing Pt coils, and thus hold great promise as an efficient and inexpensive endovascular coil material.

2. Experimental

2.1 Formation of Pt-coated nanofibers

The electrospinning precursor was prepared by mixing polyacrylonitrile [PAN, (C₃H_{3.5}N)_n; M_w = 150 kDa; Sigma-Aldrich] with *N,N*-dimethyl formamide (DMF). PAN pellets were dissolved in DMF at the concentration of 8 wt%. The solution was stirred

for 24 h at room temperature to completely dissolve the pellets. Next, the 8 wt% PAN solution was electrospun at a fixed flow rate, Q , of 160 $\mu\text{L h}^{-1}$ (Legato 100, KDS). The DC voltage, V , used was 6.0–6.5 kV (EL20P2, Glassman High Voltage Inc.), and the nozzle-to-substrate distance was 13 cm. This yielded PAN nanofibers. Next, pellets of the well-known biodegradable polymer polycaprolactone^{27,28} [PCL, (C₆H₁₀O₂)_n; M_n = 80 kDa; Sigma-Aldrich] were dissolved in an acetic acid/formic acid mixture (with the volume ratio of 3 : 1) at 15 wt% concentration. The PCL solution was then electrospun at a fixed flow rate, Q , of 85 $\mu\text{L h}^{-1}$ (Legato 100, KDS). The DC voltage, V , used was 7.5 kV (EL20P2, Glassman High Voltage Inc.). This yielded PCL nanofibers. Table 1 lists the details of the electrospinning process.

The electroplating solution was prepared by mixing a Pt HT concentrate (80 mL, Pt 50 g L⁻¹, HanTech PMC) and de-ionized (DI) water (4200 mL). The solution was stirred for 24 h at room temperature. Next, a few-nm-thick layer of Pt was formed on the PAN nanofibers by sputtering to ensure that their conductivity was high enough to allow for electroplating. The sputtered nanofibers were then electroplated under the conditions listed in Table 2. A Pt plate and the Pt-sputtered PAN nanofibers were used as the anode and cathode, respectively, and were immersed completely in the electroplating solution.

Fig. 2 shows the procedure used to form the Pt-coated nanofibers, which were then tested in a microfluidic channel. The nanofibers were electrospun onto a hollow rectangular copper frame. Next, the nanofibers were electroplated with Pt. The Pt-coated nanofiber mats were then yarned to a thick-

Table 1 Operating conditions for the electrospinning process

Items	Conditions	
	PAN	PCL
Applied voltage [V]	6.0–6.5	7.5
Flow rate [$\mu\text{L h}^{-1}$]	160	85
Nozzle-to-substrate distance [cm]	13	13
Electrospinning time [min]	20	60

Table 2 Operating conditions for the electroplating process

Items	Conditions
The electric current [A]	1
Electrode size [cm × cm]	3 × 3
Distance between electrodes [cm]	3
Electroplating time [s]	60

ness of the order of 250 μm , which is similar to that of commercial Pt coils. Yarning was performed by rolling and twisting the produced Pt mats. The thickness of the yarned cylindrical “rope” was determined based on the number of initial

nanofiber mats; the greater the mat size, the thicker was the yarning rope.

2.2 Permeability measurements

A Y-shaped channel was used for the permeability measurements. Fig. 3 shows the Y-type channel used, which had two outlets at its ends. One of the channels had a storage disk (5 mm in diameter) to mimic an aneurysmal SAH; the fabricated nanofibers were inserted into this channel. All the channel branches had a cross-sectional diameter of 1 mm. The fluid used for the measurements was prepared by dissolving polyvinyl alcohol [PVA-1500, practical grade, $(\text{C}_2\text{H}_4\text{O})_n$; Duksan Pure Chemicals Co. Ltd] in DI water in a concentration of

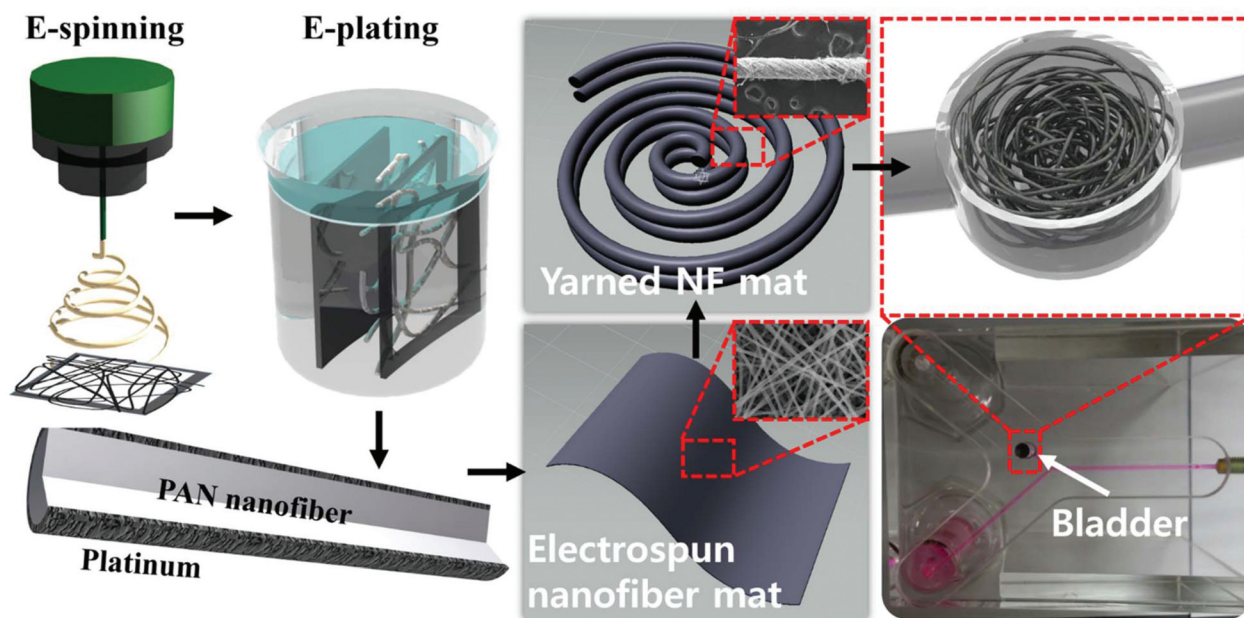


Fig. 2 Fabrication of Pt-coated nanofibers via electrospinning (the utmost left) and electroplating (second from the left). The nanofibers were yarning and inserted within a model aneurysm bladder in a microfluidic channel for permeability measurements, as is schematically shown in the four inter-related images on the right.

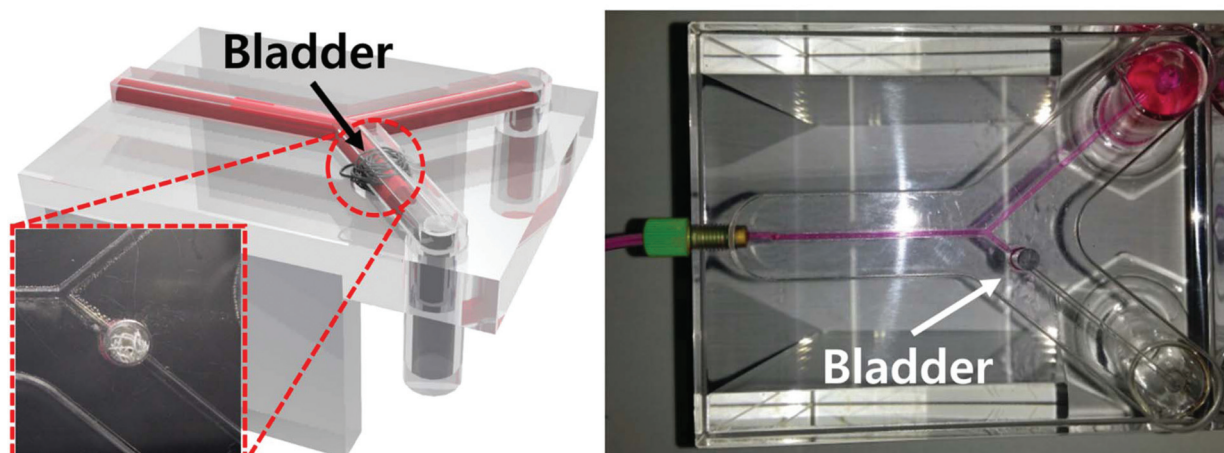


Fig. 3 Y-type microfluidic channel used for permeability measurements. Sketch is shown on the left, and the photograph is on the right.

5 wt% to mimic blood with a relatively high viscosity of 3 cP. The fluid was colored with the dye Rhodamine-B to allow for easy visualization.

It was expected that, in the case where complete channel blockage was achieved once a sufficient number of the nanofibers had been inserted in the storage disk (bladder) present in one of the channel branches, all the supplied fluid would flow into the other channel branch. This scenario is depicted in Fig. 3 (right). A syringe pump connected to the left inlet was used to drive the flow in the Y-type channel at flow rates of 0.5, 1.0, and 2.0 mL min⁻¹.

3. Results and discussion

3.1 Morphology of nanofibers

The morphologies of each fiber type were determined using a high-resolution SEM (HR-SEM) system (XL30 SFEG, Phillips Co., Holland) at 15 kV. Fig. 4 shows scanning electron microscopy (SEM) images of the electrospun nanofibers, the electroplated nanofibers, a commercial Pt coil, and the yarned ropes. The diameter of nanofibers in each case was measured by I-Measure 3 image analysis program. It can be seen from Fig. 4a that the cross-sectional diameter of the electrospun

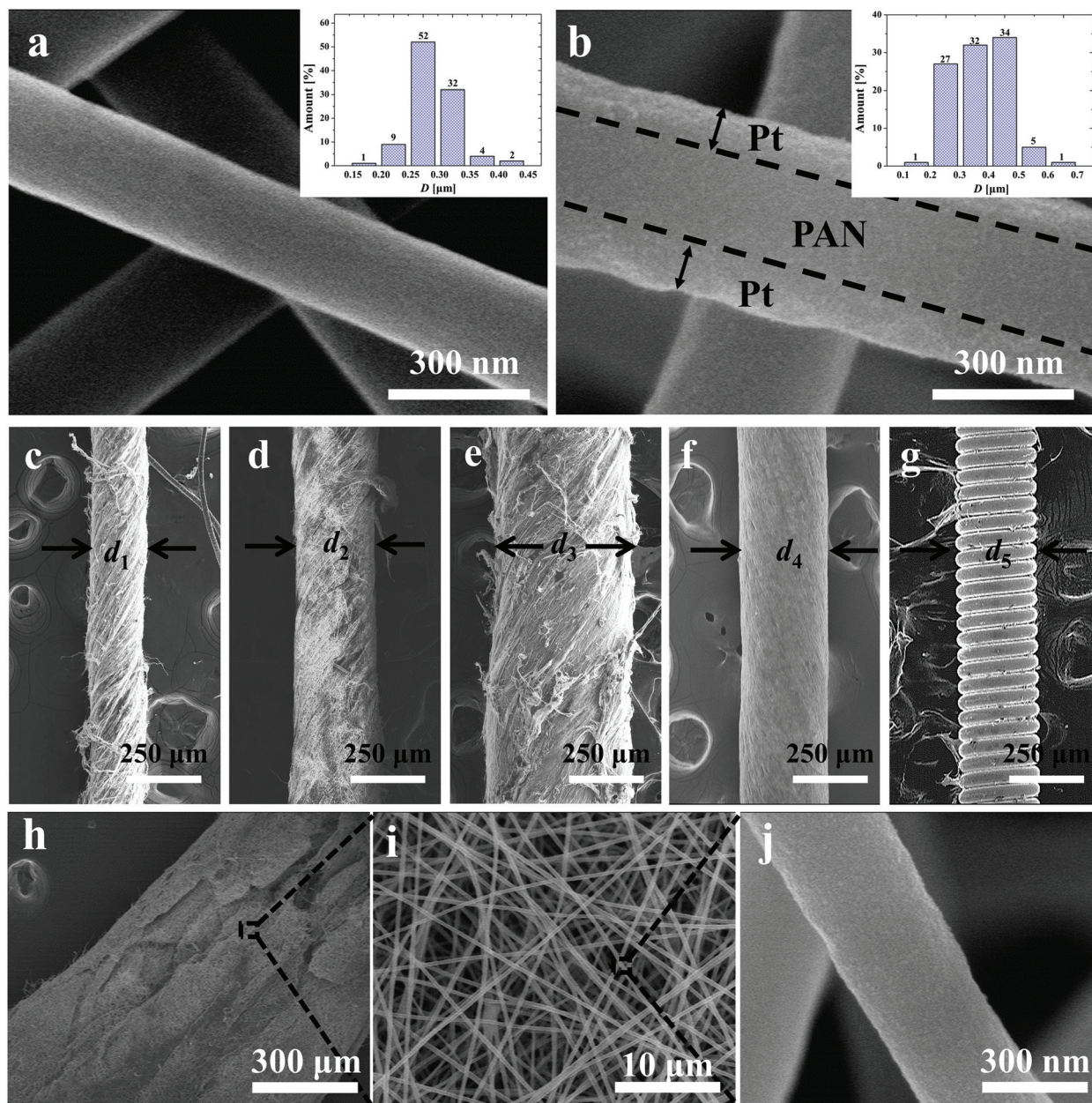


Fig. 4 SEM images of (a) pristine PAN nanofibers; (b) pristine Pt-plated PAN nanofibers; (c)–(e) yarned Pt-coated PAN nanofibers, with yarn having thicknesses of 150, 250, and 500 μm, respectively; (f) yarned PCL nanofibers; (g) commercial Pt coil; and (h)–(j) magnified images of yarned Pt-coated nanofibers.

nanofibers is in the 0.15–0.45 μm range. These PAN nanofibers were electroplated with Pt, which increased their cross-sectional diameter to 0.197–0.7 μm , as shown in Fig. 4b. It should be noted that PAN in the core was fully covered by Pt, which significantly diminished the risk of its exposure to blood vessel.²⁶ These Pt-coated nanofibers were then yarned into a cylindrical rope. Depending on the number of parallel Pt-coated nanofiber mats used to form the yarn, its thickness was in the 150–500 μm range, which is similar to that of commercial Pt coils, as can be seen from Fig. 4c–e. Fig. 4f shows the yarned PCL nanofibers, which formed the yarn with a thickness of 250 μm . Note that electrospinnable biodegradable polymers such as PCL,^{29,30} poly(L-lactide-co-glycolide) (PLGA),³¹ polyglycolic acid (PGA)³² can be also used as potential materials of the core nanofibers, albeit their metal plating is still an open question deserving research in future. Fig. 4g shows a commercial Pt coil, which has a thickness of approximately 250 μm . Fig. 4i is a magnified image of the spot marked in Fig. 4h on a yarn having a thickness of nearly 800 μm . Similarly, a higher-magnification of the yarn in Fig. 4i is shown in Fig. 4j; the nanofibers in the yarn resemble the original Pt-coated nanofibers shown in Fig. 4b.

3.2 Permeability measurements

Fig. 5 shows the PVA fluid flowing through the Y-type microfluidic channel. The fluid is collected at the two outlets (L and R). It should be emphasized that the fluid arrived first in the right container, because the presence of the storage disk (bladder) in the left channel caused a time delay of 10 s before the fluid could arrive in the left container even when there were no nanofiber yarns inserted in the disk (*i.e.*, $N = 0$). However, the difference in the fluid volumes in the left and right containers owing this 10 s delay was negligible because the bladder size was small. The flow rate of the syringe pump was set to be 1 mL min^{-1} . Thus, the total fluid volume collected over a period of 10 min was 10 mL. As a result, the ultimate total volume of the fluid in the left and right containers was 10 mL. Fig. 5a and b are top-view images of the apparatus; a circular disk containing the yarned nanofibers ($N = 1$, where N is the number of inserted yarned ropes of the same length) is located within the left (L) branch of the channel, while the right (R) channel is empty and free of obstructions. Fig. 5a and b are snapshots taken at 30 s and 180 s, respectively, after the start of fluid injection by the syringe pump. Initially, the flow in the left channel is obstructed because of the yarned nanofiber rope ($N = 1$) in the bladder. However, because the bladder is not completely filled, eventually the fluid flows through the left channel. All experiments using Y type microfluidic channels were performed three times in each case and the average values of the results were used.

The effect of the number of nanofiber yarns inserted in the storage disk, N , can be seen in Fig. 5c. As the number of the yarned fibers (ropes of the same length) was increased, the flow through the left channel became restricted, and the flow rate decreased. It should be emphasized that the image in the second row in Fig. 5c corresponds to the case shown in Fig. 5a

and b, wherein there is a minor obstruction in the flow pathway of the left channel owing to the insertion of a single nanofiber yarn ($N = 1$). Therefore, the amount of fluid collected in the left outlet is smaller than that collected in the right outlet. The difference in the amounts of fluid collected at the outlets became significant with an increase in the number of inserted nanofiber yarns, N , with the flow in the left channel being blocked completely for $N = 4$, and all the fluid flowing only through the right channel, as can be seen from the lowest image in Fig. 5c.

Fig. 5d shows the permeability (K) of the disk in the left channel as calculated using the Poiseuille equation for the channel sections and Darcy's law for the storage disk stuffed with the nanofiber yarns. The schematic used for this calculation is shown in Fig. 6.

The lower channel in the sketch in Fig. 6 comprises three distinct parts, namely, the channel itself, which has length l_1 ; the storage disk (which was stuffed with the nanofiber yarns) of length l , and the rest of the channel, whose length is l_2 . The flow through the stuffed storage disk is governed by Darcy's law, which is given by eqn (2), whereas the flow in the original channel sections is Poiseuille flow, as described by eqn (1) and (3)

$$Q_1 = \frac{\pi R^4}{8\mu} \cdot \frac{(P - P_1)}{l_1} \quad (1)$$

$$Q_1 = \frac{K}{\mu} \cdot \frac{(P_1 - P_2)}{l} \cdot \pi R^2 \quad (2)$$

$$Q_1 = \frac{\pi R^4}{8\mu} \cdot \frac{(P_2 - P_{\text{atm}})}{l_2} \quad (3)$$

These equations account for the fact that the volumetric flow rate in all the sections of the lower part of the Y-like channel in Fig. 6 is the same and equal to at Q_1 . The cross-sectional radii of the original channel sections are denoted as R . Further, μ is the fluid viscosity; P is the pressure at the bifurcation point; P_1 and P_2 , respectively, are the pressures at the entrance and exit of the storage disk; and P_{atm} is the pressure at the channel exit (atmospheric). The highest pressure imposed on the channel before the bifurcation of the fluid is denoted as P_{pump} in Fig. 6. Finally, K is the permeability of the storage disk in eqn (2).

After bifurcation, fluid flow in the upper branch (see Fig. 6), which has a volumetric flow rate of Q_2 is described by the Poiseuille law as follows:

$$Q_2 = \frac{\pi R^4}{8\mu} \cdot \frac{(P - P_{\text{atm}})}{L_2} \quad (4)$$

In addition, the total volumetric flow rate for the flow from the pump, Q_0 , is

$$Q_0 = Q_1 + Q_2 \quad (5)$$

Also, the geometric conditions mean that

$$l_1 + l_2 + l = L_2 \quad (6)$$

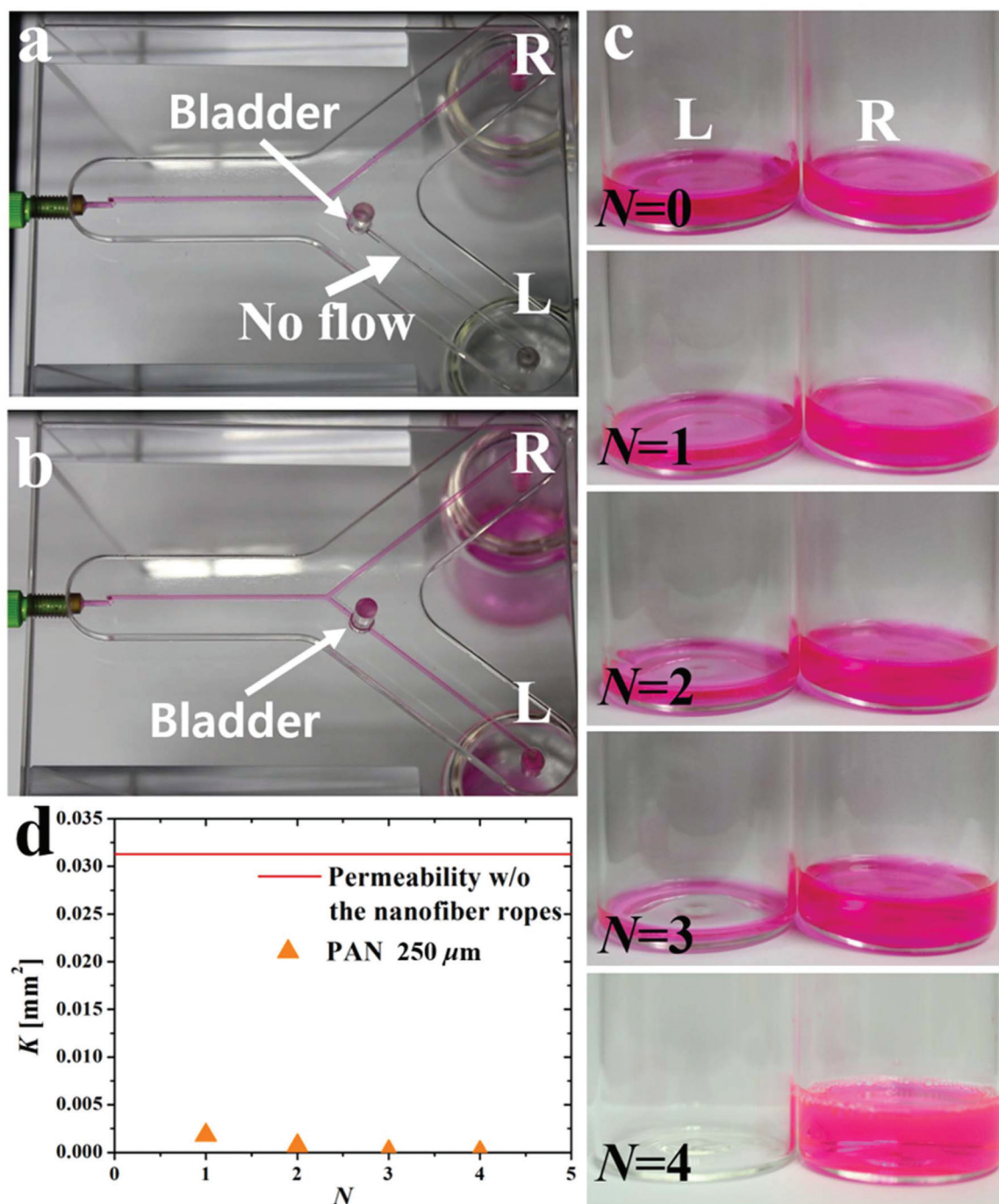


Fig. 5 Barrier effect of 250 μm nanofibers in Y-type channel. Panels (a) and (b) are the top-view images of the apparatus; a circular disk contains the yarned nanofibers ($N = 1$, with N being the number of inserted yarned ropes of the same length). (c) The difference in the amounts of fluid collected at the outlets with an increase in the number of inserted nanofiber yarns, N . (d) Permeability (K) of the disk in the left channel.

Eqn (1)–(6) yield the permeability of the stuffed storage disk in the following form:

$$K = \frac{Q_1 l}{Q_0 L_2 + Q_1 (l - 2L_2)} \frac{R^2}{8}. \quad (7)$$

If the disk were to be empty, $Q_1 = Q_2 = Q_0/2$, and eqn (7) would be reduced to $K = R^2/8$, as expected for Poiseuille flow-based permeability. It should be noted that, when the disk is completely blocked by the inserted nanofibers, the flow rate in the channel without the disk, Q_2 , is equal to the total flow rate,

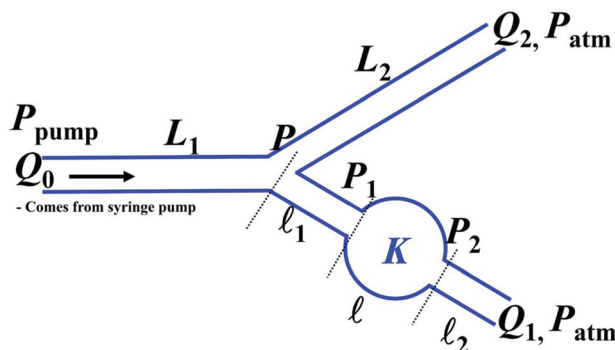


Fig. 6 Schematic of flow in Y-type channel used for permeability calculation. All the notations are explained in the text.

Q_0 , while the flow rate through the disk-containing branch, Q_1 , is 0. Then, the disk permeability, k , is 0 according to eqn (7). In addition, the relationship between the pump pressure, P_{pump} , and the total volumetric flow rate, Q_0 , is as follows:

$$P_{\text{pump}} = P_{\text{atm}} + \frac{Q_0 8 \mu L_1}{\pi R^4} + \frac{Q_2 8 \mu L_2}{\pi R^4}. \quad (8)$$

The permeability values shown in Fig. 5d were obtained using eqn (7). It can be seen that, when the number of inserted yarned ropes, N , is 4, the disk becomes practically impermeable.

Fig. 7 shows the permeability values as measured under different conditions. Fig. 7a shows the effect of the total flow rate, Q_0 , on K for an uncoated PAN fiber yarn with a diameter, d , of 250 μm . As expected, for a fixed N value, the permeability does not change even if Q_0 is doubled or quadrupled. Indeed, according to eqn (7), the permeability, K , is practically independent of Q_0 ; this was confirmed by the experimental data. Fig. 7b shows the effect of the diameter ($d = 150, 250$, and 500 μm) of the uncoated PAN yarn on K . It should be emphasized that the yarns with diameters, d , of 150, 250, and 500 μm had lengths of 27, 12, and 3 cm, respectively, in order to ensure that the volume was the same in each case. The yarn with the smallest diameter exhibited the lowest permeability; this was especially apparent when $N = 1$. Furthermore, this pattern persisted at $N = 2$. On the other hand, the permeability was almost zero for all the yarn diameters at $N = 3$. Yarns composed of smaller fibers will have a higher surface area. Thus, the drag force acting on the flow will be the greatest in the case of the

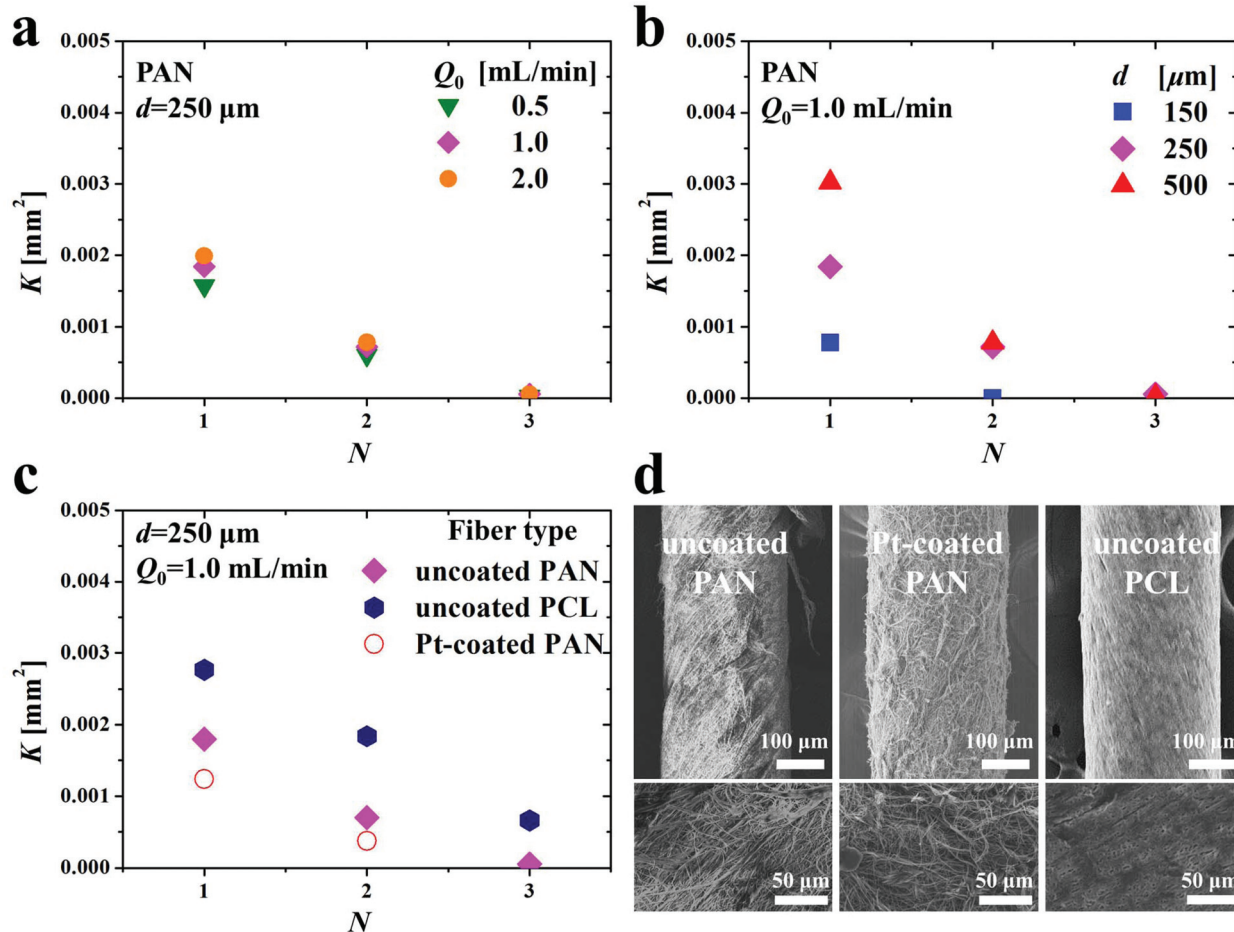


Fig. 7 Variation in permeability, K , with (a) changes in total flow rate Q_0 ; (b) yarned PAN fiber diameter, d ; (c) and yarned fiber type (i.e., uncoated PAN, uncoated PCL, and Pt-coated PAN). (d) SEM images of yarned ropes of uncoated PAN, Pt-coated PAN, and uncoated PCL fibers.

fibers with the smallest diameter and the corresponding permeability will be the lowest. Fig. 7c shows the difference in the permeabilities measured for the different yarn types (yarns composed of the uncoated PAN fibers, uncoated PCL fibers, and Pt-coated PAN fibers) for the same diameter and a fixed flow rate. The results show that the yarn composed of the Pt-coated fibers was the most efficient in blocking the flow and exhibited the lowest permeability, while the yarn composed of the uncoated PCL fibers was the poorest. This effect of the material type can probably be attributed to the surface texture of the individual fibers in the yarn and the yarn as a whole. Thus, the material with the highest surface roughness and area, that is, the yarn with the Pt-coated PAN fibers, imposed the greatest drag on the flow, and thus resulted in the greatest decrease in the permeability.

3.3 Wettability measurements

The surface wettability of a material probably plays a role in determining its permeability to fluids. If the fiber (and thus, the yarn) surfaces were to be hydrophobic, fluids would not adhere to the surface. This, in turn, would facilitate the through flow of fluids and result in a higher permeability. On the other hand, in the case of hydrophilic fibers (and thus, hydrophilic yarn) surfaces, fluids would adhere to the fibers, resulting in a higher drag and reduced permeability. Fig. 8 compares the wettabilities of the uncoated PAN, uncoated PCL, and Pt-coated PAN fiber mats. Water contact angles on the mats were measured using a goniometer. A high-speed camera (Phantom 9.1, Vision Research, Inc.) was used to photograph the water drop shape on the film at 5 FPS. The

angles were measured by I-Measure 3 image analysis program. In each case, a water drop ($\sim 5 \mu\text{L}$) was placed on the nanofiber mat and the contact angle was checked from 0 to 30 s. After 20 s, the water absorption stopped and the static state was achieved. Measurements of the contact angle were performed three times in each case and Fig. 8 shows the most reliable results. The porosities of all three types of mats are similar because the mat collection times, fiber sizes, and mat thicknesses were the same. The uncoated PAN and Pt-coated PAN fiber mats show similar wettabilities, with the Pt-coated PAN mats being the more wettable ones. On the other hand, the uncoated PCL mats are more hydrophobic. These observations are consistent with the permeability changes shown in Fig. 7c. Thus, the greater the hydrophobicity, the higher should be the permeability, as was seen in case of the uncoated PCL fibers.

4. Theoretical analysis

4.1 Theoretical model

The endovascular treatment of brain aneurysms by coil embolization poses the following hydrodynamic problem: which part of the volumetric flow in the pipe (blood vessel) passes through an adjoining cavity (aneurysm) having its inlet from the pipe and its outlet to the pipe (with there being no pipe interruption), when the cavity is filled with a porous medium and the flow is Darcy-like filtration flow determined by the permeability of the cavity? A solution of this problem would also be useful from a medical viewpoint, where the first aim is to

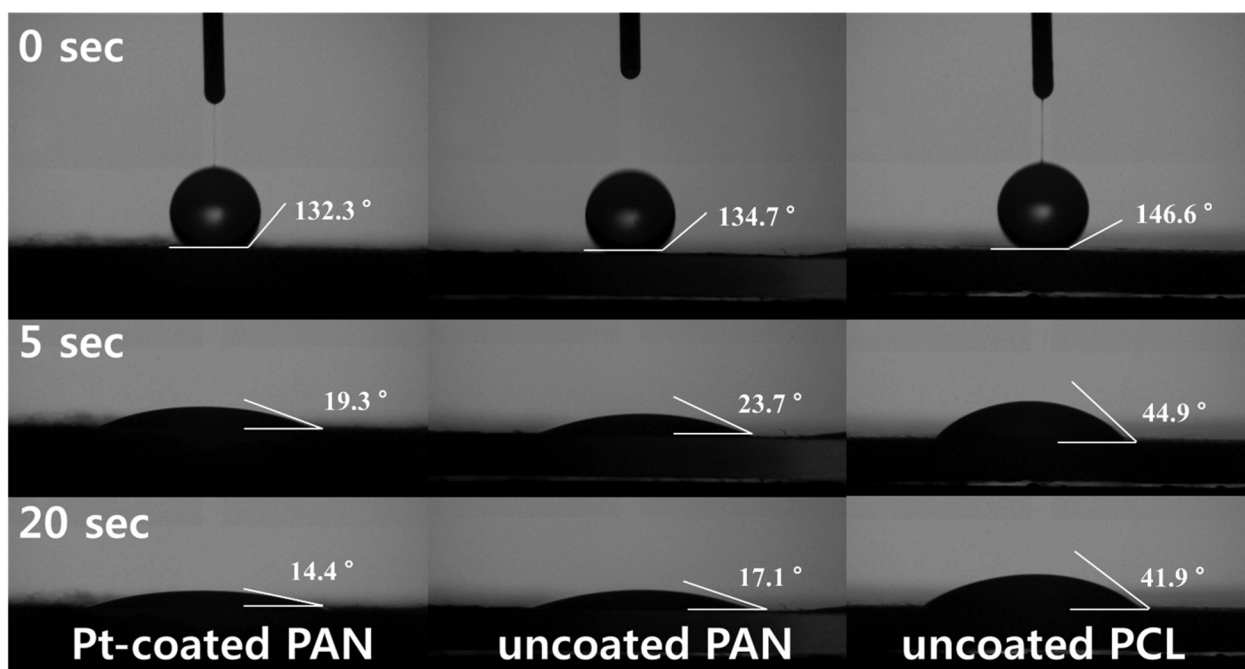


Fig. 8 Water advancing contact angles on various fiber mats: the left-hand side column is for Pt-coated PAN, the middle column is for uncoated PAN, and the right-hand side column is for uncoated PCL.

reduce the permeability of the cavity (*i.e.*, to treat the aneurysm) by installing coils and to significantly suppress the internal flow, which can result in aneurysm rupture with severe consequences. On the other hand, as a second aim, coiling should be minimized in order to reduce cost. This, in conjunction with the first aim, becomes an optimization problem.

The hydrodynamics of blood flow (hemodynamics) in a brain blood vessel with an adjoining aneurysm have been studied in the past based on direct numerical simulations of the Navier–Stokes equations for three-dimensional morphologies resembling the actual ones.^{33–35} However, these studies did not consider the non-Newtonian effects arising in the blood flow, which is a plausible approximation for this class of problems. The endovascular treatment of aneurysms involves the installation of multiple Pt coils to reduce the permeability of the aneurysm. The cost of the coils and the treatment, in general, is so high that a reasonable trade-off is desirable to minimize the number of the coils needed, while ensuring that the desired permeability is achieved. This issue poses an important and interesting fluid mechanical problem. In the case where multiple coils are installed in an aneurysm, the detailed internal geometry would not only be unknown but would also be difficult to simulate numerically.^{34,35} Therefore, reducing the aneurysm permeability through an endovascular treatment (*i.e.*, by using the appropriate number of coils of suitable shape) has attracted attention from a filtration viewpoint.^{25,33} Such an approach requires solving a conjugate problem based on the Navier–Stokes equations for flow in a single blood vessel coupled with filtration (*i.e.*, Darcy-law-related) flow in the adjacent aneurysm with coils installed.

A model describing the primary hydrodynamics characteristics of brain aneurysms with installed Pt embolic coils is shown in Fig. 9. This model sheds light on the hydrodynamic aspects of the problem at hand. For this planar

problem, the aneurysm is the circular bulge ABCDE formed on top of an adjoining blood vessel. Blood flow from the blood vessel, which is described by its volumetric flow rate, Q_0 , can partially enter the aneurysm through opening “ab” with an unknown volumetric flow rate, Q_2 , while the rest of the blood in the blood vessel after the partition flows with the volumetric flow rate $Q_1 = Q_0 - Q_2$. The blood flowing through the aneurysm leaves it through opening “cd” and enters the blood vessel again. Blood flow inside the aneurysm filled with the Pt embolic coils is considered to be a filtration flow through a medium with permeability K , whereas in the blood vessel, the flow is assumed to be viscous Poiseuille flow. The next step is to determine the blood partition ratio, that is, the volumetric flow rate through the aneurysm, Q_2 , and to minimize it to the appropriate level by reducing the permeability, K , which is determined by the number of Pt embolic coils installed as well as their shape.²⁵

In Fig. 9, the Cartesian coordinates x and y as well as the complex variable $z = x + iy$ are introduced and rendered dimensionless by the aneurysm radius R . Therefore, the dimensionless radius of the aneurysm in this figure is 1. The velocity field, \mathbf{v} , of the filtration flow within the aneurysm is related to the pressure field, p , by Darcy’s law, $\mathbf{v} = -(K/\mu)\nabla p$, where μ is the viscosity of blood. This suggests that the flow possesses potential $\varphi = -(K/\mu)p$. Since the filtration flow satisfies the continuity equation, the potential φ satisfies the Laplace equation. As is usually the case, the potential, as a harmonic function, satisfies the Laplace equation not only on the physical complex plane z , but also on any other complex plane onto which the plane z has been mapped conformally. In the present case, it is convenient to map the interior of the circle in the z plane onto the complex upper half-plane $\omega = \xi + i\eta$, as depicted in Fig. 10. This is achieved by using the mapping function $z = (i - \omega)/(i + \omega)$, which is equivalent to the following coordinate transformation:

$$\xi = \frac{2y}{(1+x)^2 + y^2}, \quad \eta = \frac{(1-x^2-y^2)}{(1+x)^2 + y^2}, \quad (9)$$

when point B is mapped onto the point on the horizontal axis $\xi = -1$, point C is mapped onto $\xi = 0$, point D is mapped onto $\xi = 1$, and points A and E are mapped to infinity.

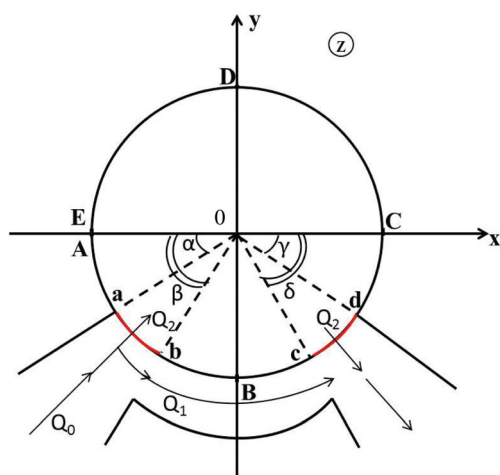


Fig. 9 Schematic of blood vessel with adjoining aneurysm in physical plane $z = x + iy$; i is imaginary unit.

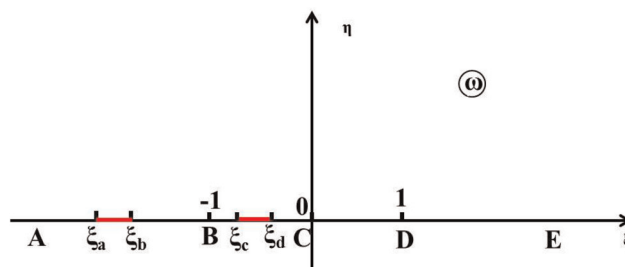


Fig. 10 Aneurysm mapped to upper half-plane $\omega = \xi + i\eta$.

The ξ coordinates of points a, b, c, and d also mapped onto the horizontal axis on the ω -plane and are given by the following expressions:

$$\begin{aligned}\xi_a &= -\frac{\sin \alpha}{(1 - \cos \alpha)}, & \xi_b &= -\frac{\sin \beta}{(1 - \cos \beta)}, \\ \xi_c &= -\frac{\sin \delta}{(1 + \cos \delta)}, & \xi_d &= -\frac{\sin \gamma}{(1 + \cos \gamma)},\end{aligned}\quad (10)$$

(see Fig. 10). The angles α , β , γ , and δ , which range from 0° to 90° , are depicted in Fig. 9.

It is assumed that, in the ω -plane, the fluid flows into the upper half-plane through section $\xi_a\xi_b$ with velocity V_0 and subsequently flows from the upper half-plane with velocity $-V_1$ through section $\xi_c\xi_d$; in both cases, the flow is normal to the domain boundary. Velocity V_1 is such that the condition for volumetric balance $V_1(\xi_d - \xi_c) = V_0(\xi_b - \xi_a)$ is fulfilled. Accordingly, there exists a corresponding inflow to the aneurysm and an outflow from it in the z -plane. The complex potential is introduced as $\chi = \varphi + i\psi$, with ψ being the stream function. Accordingly, the conjugate velocity is given by $d\chi(z)/dz = \bar{V}(z) = \bar{V}(\omega)[-2i/(1+z^2)]$, where $\bar{V}(\omega) = d\chi(\omega)/d\omega$. We denote the ξ and η components of the velocity on the ω -plane as U and V , respectively, and introduce the analytic function $i\bar{V}(\omega) = V + iU$. The real part of this analytic function is given, as described above, at the real axis of the ω -plane. Thus, it can be found for the entire upper half-plane using the Poisson integral,³⁶ as shown below:

$$\begin{aligned}V(\xi, \eta) &= \frac{\eta}{\pi} \left[V_0 \int_{\xi_a}^{\xi_b} \frac{d\zeta}{(\zeta - \xi)^2 + \eta^2} - V_1 \int_{\xi_c}^{\xi_d} \frac{d\zeta}{(\zeta - \xi)^2 + \eta^2} \right] \\ &= \frac{V_0}{\pi} \left\{ \arctan\left(\frac{\xi_b - \xi}{\eta}\right) - \arctan\left(\frac{\xi_a - \xi}{\eta}\right) - \frac{(\xi_b - \xi_a)}{(\xi_d - \xi_c)} \right. \\ &\quad \times \left. \left[\arctan\left(\frac{\xi_d - \xi}{\eta}\right) - \arctan\left(\frac{\xi_c - \xi}{\eta}\right) \right] \right\}.\end{aligned}\quad (11)$$

Since V and U are related by the Cauchy–Riemann conditions [*i.e.*, $\partial V/\partial \xi = \partial U/\partial \eta$ and $\partial V/\partial \eta = -\partial U/\partial \xi$], one can easily find U on the upper half-plane ω and hence find the analytic function $i\bar{V}(\omega)$ as well as $\bar{V}(\omega)$, as shown below:

$$\bar{V}(\omega) = -\frac{V_0}{\pi} \left[\ln\left(\frac{\omega - \xi_b}{\omega - \xi_a}\right) - \left(\frac{\xi_b - \xi_a}{\xi_d - \xi_c}\right) \ln\left(\frac{\omega - \xi_d}{\omega - \xi_c}\right) \right]. \quad (12)$$

It should be emphasized that eqn (12) can be determined directly from the expression for the Schwarz integral for the upper half-plane, which can be used to determine any analytical function. Thus, in this particular case, $\bar{V}(\omega)$ if found based on its imaginary part on the real axis, ξ , as $\bar{V}(\omega) = (-1/\pi) \int_{-\infty}^{\infty} V(\xi)/(\xi - \omega) d\xi + B$, where the real constant B can be ignored in the present case.

The complex potential is found *via* the integration of eqn (12) as

$$\chi(\omega) = -\frac{V_0}{\pi} \left\{ \Phi(\omega, \xi_b) - \Phi(\omega, \xi_a) - \left(\frac{\xi_b - \xi_a}{\xi_d - \xi_c}\right) [\Phi(\omega, \xi_d) - \Phi(\omega, \xi_c)] \right\} \quad (13)$$

where the function $\Phi(\omega, \bullet)$ is defined as

$$\Phi(\omega, \bullet) = (\omega - \bullet)[\ln(\omega - \bullet) - 1] \quad (14)$$

It should be emphasized that the complex potential $\chi(z)$ in the z -plane is obtained from eqn (13) and (14) by substituting the reverse mapping function:

$$\omega = i\left(\frac{1-z}{1+z}\right). \quad (15)$$

The flow and pressure fields in the aneurysm are found using the imaginary and real parts of the complex potential $\chi(z)$, that is, from $\psi(x, y)$ and $p(x, y) = -\mu\varphi(x, y)/K$.

4.2 Theoretical results and discussion

Several examples of the flows predicted by eqn (13)–(15) on the physical plane are depicted in Fig. 11–13. In particular, as can be seen from Fig. 11a–13a, the strongest flows correspond to the deep-blue area (with the lowest negative values of ψ —these correspond to the definition of the stream function in the present case). These areas span the inlet and outlet of the aneurysm along the shortest arc. Fig. 11b–13b show the corresponding pressure fields [$Kp/\mu = -\varphi(x, y)$], with the highest pressure values (red color) corresponding to the inlet and the lowest values (blue color) corresponding to the outlet.

Eqn (13) and (14) yield $\psi_a = \psi_d = 0$, and $\psi_b - \psi_a = \psi_c - \psi_d = -V_0(\xi_b - \xi_a)$, which expresses the overall mass balance between the inflow and outflow through the aneurysm openings. Using eqn (13) and (14) and by recovering the length scale, R , one can find the pressure drop along the streamline spanning points a and d within the aneurysm:

$$p_a - p_b = \frac{\mu V_0 R}{K\pi} F(\xi_a, \xi_b, \xi_c, \xi_d), \quad (16)$$

where the dimensionless function $F(\xi_a, \xi_b, \xi_c, \xi_d)$ is defined as

$$\begin{aligned}F(\xi_a, \xi_b, \xi_c, \xi_d) &= (\xi_a - \xi_b)[\ln(\xi_b - \xi_a) - 1] - (\xi_d - \xi_b) \\ &\quad \times [\ln(\xi_d - \xi_b) - 1] + (\xi_d - \xi_a)[\ln(\xi_d - \xi_a) - 1] \\ &\quad - \left(\frac{\xi_b - \xi_a}{\xi_d - \xi_c}\right) \times \left\{ (\xi_a - \xi_d)[\ln(\xi_d - \xi_a) - 1] \right. \\ &\quad - (\xi_a - \xi_c)[\ln(\xi_c - \xi_a) - 1] + (\xi_d - \xi_c) \\ &\quad \times [\ln(\xi_d - \xi_c) - 1] \left. \right\}\end{aligned}\quad (17)$$

On the other hand, the same pressure difference as in eqn (16) is sustained by the planar Poiseuille flow in the model blood vessel between points a and d, while based on the Poiseuille law. Accordingly one finds that

$$p_a - p_d = \frac{12\mu R(\pi - \gamma - \alpha)}{H^3} Q_1 \quad (18)$$

where H is the size of the cross-section of the blood vessel.

Then, eqn (16)–(18) yield the following expression for the velocity of the inflow into the aneurysm in the ω -plane, V_0 , and

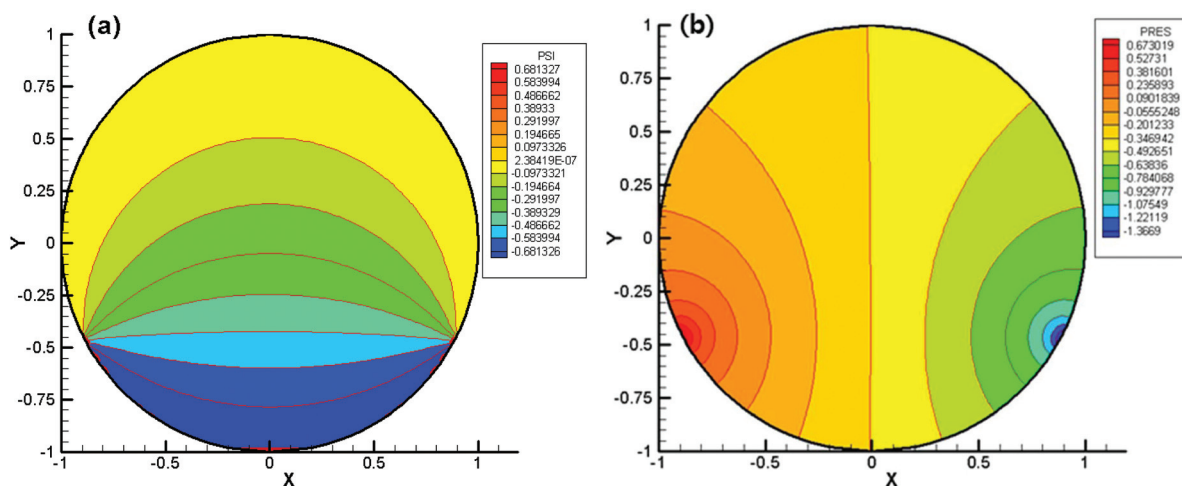


Fig. 11 (a) Flow field $[\psi(x, y)]$ with several streamlines highlighted in different colors. (b) Corresponding pressure field $[Kp/\mu = -\varphi(x, y)]$. Angle values are: $\alpha = 25^\circ$, $\beta = 30^\circ$, $\gamma = 25^\circ$, and $\delta = 30^\circ$.

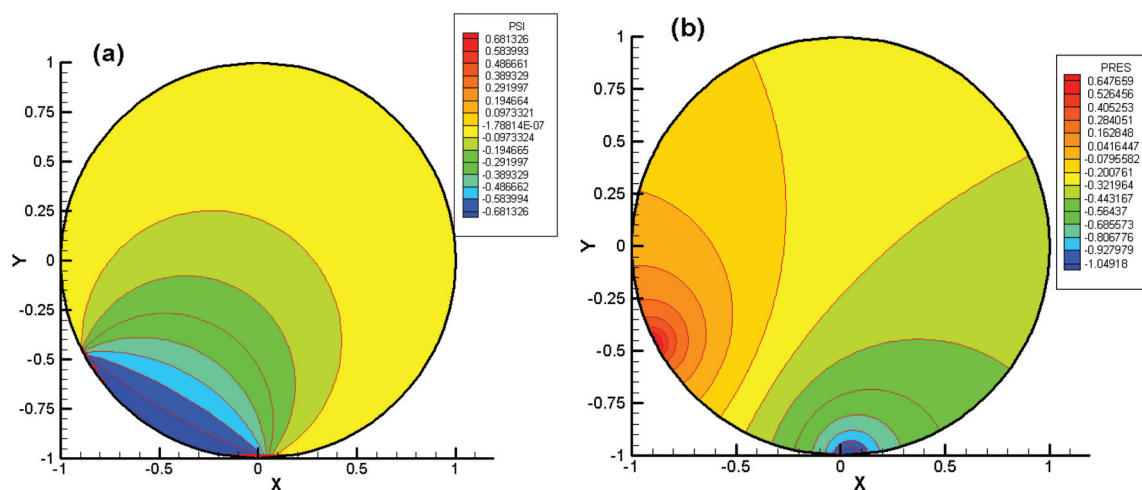


Fig. 12 (a) Flow field $[\psi(x, y)]$ with several streamlines highlighted in different colors. (b) Corresponding pressure field $[Kp/\mu = -\varphi(x, y)]$. Angle values are: $\alpha = 25^\circ$, $\beta = 30^\circ$, $\gamma = 85^\circ$, and $\delta = 90^\circ$.

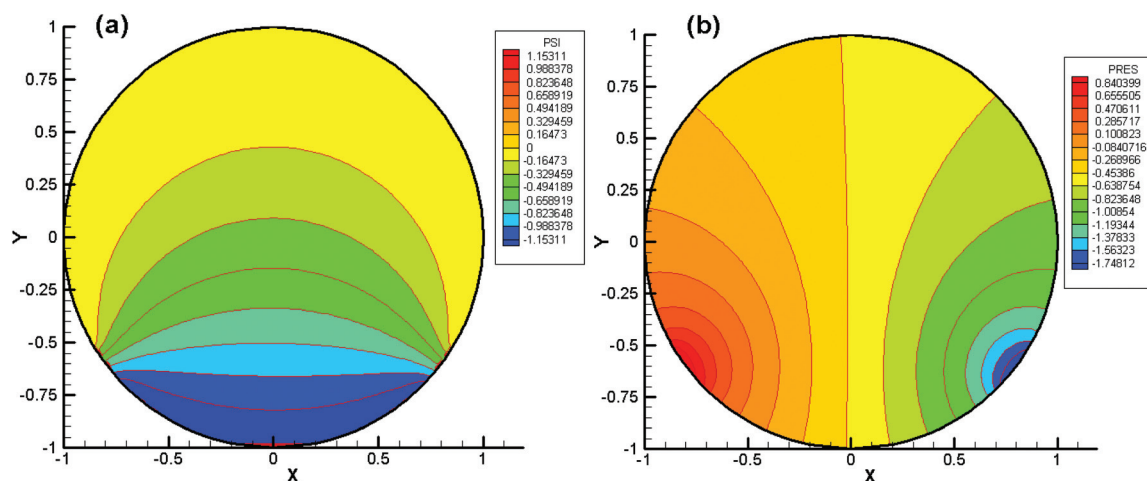


Fig. 13 (a) Flow field $[\psi(x, y)]$ with several streamlines highlighted in different colors. (b) Corresponding pressure field $[Kp/\mu = -\varphi(x, y)]$. Angle values are: $\alpha = 30^\circ$, $\beta = 45^\circ$, $\gamma = 30^\circ$, and $\delta = 45^\circ$.

the partitioning of the volumetric flow rate between the aneurysm and the blood vessel:

$$V_0 = \frac{Q_0}{W_* + R(\xi_b - \xi_a)}, \quad (19)$$

$$Q_1 = Q_0 \frac{W}{W + (\xi_b - \xi_a)}, \quad (20)$$

$$Q_2 = Q_0 \frac{(\xi_b - \xi_a)}{W + (\xi_b - \xi_a)}, \quad (21)$$

with the dimensional W_* and its dimensionless counterpart, W , being given by the following expressions:

$$W_* = WR, \quad W = \frac{1}{12\pi(\pi - \gamma - \alpha)} \frac{H^3/R}{K} F(\xi_a, \xi_b, \xi_c, \xi_d). \quad (22)$$

Eqn (20)–(22) yielded the following values for the parameters corresponding to the three examples given above for a blood vessel-to-aneurysm permeability ratio $(H^3/R)/K = 1$: for Fig. 11 – $W = 0.074$, $Q_1/Q_0 = 0.086$, and $Q_2/Q_0 = 0.91$; for Fig. 12 – $W = 0.121$, $Q_1/Q_0 = 0.135$, and $Q_2/Q_0 = 0.865$; and for Fig. 13 – $W = 0.098$, $Q_1/Q_0 = 0.069$, and $Q_2/Q_0 = 0.931$. It is remarkable that, in all the cases with equal permeabilities, the influx into the aneurysm is very high, between 86.5% and 93.1%. On the other hand, for a permeability ratio of $(H^3/R)/K = 100$, that is, when the aneurysm permeability, K , is reduced by a factor of 100, one gets the following results: for Fig. 11 – $W = 7.4$, $Q_1/Q_0 = 0.905$, and $Q_2/Q_0 = 0.095$; for Fig. 12 – $W = 12.1$, $Q_1/Q_0 = 0.94$, and $Q_2/Q_0 = 0.06$; and for Fig. 13 – $W = 9.8$, $Q_1/Q_0 = 0.882$, and $Q_2/Q_0 = 0.118$. The latter set of results shows that a 100-fold decrease in the aneurysm permeability would decrease blood influx into the aneurysm to 6–12% of the total blood flux in the blood vessel.

5. Conclusions

Uncoated PAN, uncoated PCL, and Pt-coated PAN were formed by electrospinning and subsequent electroplating. The filtration flow passing through a planar model brain aneurysm was studied experimentally. Permeabilities of yarns composed of uncoated PAN, uncoated PCL, and Pt-coated PAN nanofibers were measured in order to evaluate their potential for use as replacements for Pt coils for preventing the extravasation of blood after aneurysmal subarachnoid hemorrhage. The Pt-coated PAN nanofibers exhibited the lowest permeability and thus hold the great promise for applications. The filtration flow passing through a planar model brain aneurysm was simulated for all possible connections with an uninterrupted adjacent pipe (blood vessel), and its relation to the aneurysm permeability, which would be determined by the endovascular treatment (coil embolization) performed, was established. It was observed that, when the aneurysm permeability is reduced to one-hundredth of that of the blood vessel, the filtration flow through the aneurysm is reduced to approximately 12% of the total blood flow in the blood vessel before its first connection with the aneurysm.

Conflicts of interest

There are no conflicts to declare.

Acknowledgements

This work (C0421241) was supported by Business for Cooperative R&D between Industry, Academy, and Research Institute funded Korea Small & Medium Business Administration. This research was supported by Korea University Medical-Engineering Fusion Research Grant. This research was supported by the Technology Development Program to Solve Climate Changes of the National Research Foundation (NRF) funded by the Ministry of Science, ICT & Future Planning (NRF-2016 M1A2A2936760) and NRF-2017R1A2B4005639.

References

- 1 J. I. Suarez, R. W. Tarr and W. R. Selman, *N. Engl. J. Med.*, 2006, **354**, 387–396.
- 2 J. P. Broderick, T. Brott, T. Tomsick, G. Huster and R. Miller, *N. Engl. J. Med.*, 1992, **326**, 733–736.
- 3 J. P. Broderick, T. Brott, T. Tomsick, R. Miller and G. Huster, *J. Neurosurg.*, 1993, **78**, 188–191.
- 4 F. Linn, G. Rinkel, A. Algra and J. Van Gijn, *Stroke*, 1996, **27**, 625–629.
- 5 V. Menghini, R. D. Brown, J. Sicks, W. O'fallon and D. Wiebers, *Neurology*, 1998, **51**, 405–411.
- 6 N. K. de Rooij, F. H. Linn, J. A. van der Plas, A. Algra and G. J. Rinkel, *J. Neurol., Neurosurg. Psychiatry*, 2007, **78**, 1365–1372.
- 7 T. J. Ingall, J. P. Whisnant, D. O. Wiebers and W. M. O'fallon, *Stroke*, 1989, **20**, 718–724.
- 8 J. W. Hop, G. J. Rinkel, A. Algra and J. van Gijn, *Stroke*, 1997, **28**, 660–664.
- 9 S. C. Johnston, S. Selvin and D. R. Gress, *Neurology*, 1998, **50**, 1413–1418.
- 10 T. N. Taylor, P. H. Davis, J. C. Torner, J. Holmes, J. W. Meyer and M. F. Jacobson, *Stroke*, 1996, **27**, 1459–1466.
- 11 W. C. Lee, M. C. Christensen, A. V. Joshi and C. L. Pashos, *Cerebrovasc. Dis.*, 2007, **23**, 57–65.
- 12 S. Ridwan, H. Urbach, S. Greschus, J. von Hagen, J. Esche and A. Boström, *World Neurosurg.*, 2017, **97**, 495–500.
- 13 G. Guglielmi, F. Viñuela, J. Dion and G. Duckwiler, *J. Neurosurg.*, 1991, **75**, 8–14.
- 14 A. Molyneux, R. Kerr, I. Stratton, P. Sandercock, M. Clarke, J. Shrimpton and R. Holman, *Lancet*, 2002, **360**, 1267–1274.
- 15 C. P. Derdeyn, J. D. Barr, A. Berenstein, J. J. Connors, J. E. Dion, G. R. Duckwiler, R. T. Higashida, C. M. Strother, T. A. Tomsick and P. Turski, *Am. J. Neuroradiol.*, 2003, **24**, 1404–1408.

- 16 A. Raabe, P. Schmiedek, V. Seifert and D. Stolke, *Z. Neurol.*, 2003, **64**, 99–103.
- 17 A. Qureshi, A. Hutson, R. Harbaugh, P. Stieg and L. Hopkins, *Neurosurgery*, 2004, **54**, 248–264.
- 18 J. S. McDonald, R. McDonald, J. Fan, D. F. Kallmes, G. Lanzino and H. Cloft, *Am. J. Neuroradiol.*, 2014, **35**, 164–169.
- 19 H. G. Morales, M. Kim, E. Vivas, M.-C. Villa-Uriol, I. Larrabide, T. Sola, L. Guimaraens and A. Frangi, *Am. J. Neuroradiol.*, 2011, **32**, 1935–1941.
- 20 C. A. Taschner, X. Leclerc, J.-Y. Gauvrit, A. Kerkeni, M. El-Mahdy, J.-P. Lejeune and J.-P. Pruvo, *Neuroradiology*, 2007, **49**, 761–766.
- 21 A. J. Molyneux, A. Clarke, M. Sneade, Z. Mehta, S. Coley, D. Roy, D. F. Kallmes and A. J. Fox, *Stroke*, 2012, **43**, 2544–2550.
- 22 C. G. McDougall, S. C. Johnston, A. Gholkar, S. Barnwell, J. V. Suarez, J. M. Romero, J. Chaloupka, A. Bonafe, A. K. Wakhloo and D. Tampieri, *Am. J. Neuroradiol.*, 2014, **35**, 935–942.
- 23 P. M. White, S. C. Lewis, A. Gholkar, R. J. Sellar, H. Nahser, C. Cognard, L. Forrester and J. M. Wardlaw, *Lancet*, 2011, **377**, 1655–1662.
- 24 M. Ahearne, Y. Yang and K. Liu, *Top. Tissue Eng.*, 2008, **4**, 1–16.
- 25 A. K. Johnson, A. L. Yarin and F. Mashayek, *Neurosurgery*, 2012, **71**, E1064–E1065.
- 26 S. An, Y. I. Kim, S. Sinha-Ray, M.-W. Kim, H. S. Jo, M. T. Swihart, A. L. Yarin and S. S. Yoon, *Nanoscale*, 2017, **9**, 6076–6084.
- 27 H. Kweon, M. K. Yoo, I. K. Park, T. H. Kim, H. C. Lee, H.-S. Lee, J.-S. Oh, T. Akaike and C.-S. Cho, *Biomaterials*, 2003, **24**, 801–808.
- 28 M. A. Woodruff and D. W. Hutmacher, *Prog. Polym. Sci.*, 2010, **35**, 1217–1256.
- 29 S. Sett, M. W. Lee, M. Weith, B. Pourdeyhimi and A. L. Yarin, *J. Mater. Chem. B*, 2015, **3**, 2147–2162.
- 30 S. An, J. H. Hong, K. Y. Song, M. W. Lee, S. S. Al-Deyab, J. J. Kim, A. L. Yarin and S. S. Yoon, *Cellulose*, 2017, **24**, 951–965.
- 31 W. J. Li, C. T. Laurencin, E. J. Caterson, R. S. Tuan and F. K. Ko, *J. Biomed. Mater. Res., Part A*, 2002, **60**, 613–621.
- 32 Y. You, J. H. Youk, S. W. Lee, B.-M. Min, S. J. Lee and W. H. Park, *Mater. Lett.*, 2006, **60**, 757–760.
- 33 K. S. Cha, E. Balaras, B. B. Lieber, C. Sadasivan and A. K. Wakhloo, *J. Biomech. Eng.*, 2007, **129**, 873–879.
- 34 M. H. Babiker, L. F. Gonzalez, F. Albuquerque, D. Collins, A. Elvikis and D. H. Frakes, *Ann. Biomed. Eng.*, 2010, **38**, 2293–2301.
- 35 D. M. Sforza, C. M. Putman and J. R. Cebal, *Annu. Rev. Fluid Mech.*, 2009, **41**, 91–107.
- 36 G. Polya and G. Latta, *Complex Variables*, John Wiley & Sons, New York, 1974.